Analysis of geometrical and statistical features of Lagrangian stretching in turbulent channel flow using a database task-parallel particle tracking algorithm

Perry L. Johnson,[1,*] Stephen S. Hamilton,[2] Randal Burns,[2] and Charles Meneveau[1]

[1]*Department of Mechanical Engineering and Center for Environmental and Applied Fluid Mechanics, Johns Hopkins University, 3400 N. Charles Street, Baltimore, Maryland 21218, USA*

[2]*Department of Computer Science, Johns Hopkins University, 3400 N. Charles Street, Baltimore, Maryland 21218, USA*

(Received 21 June 2016; published 23 January 2017)

An intrinsic property of turbulent flows is the exponential deformation of fluid elements along Lagrangian paths. The production of enstrophy by vorticity stretching follows from a similar mechanism in the Lagrangian view, though the alignment statistics differ and viscosity prevents unbounded growth. In this paper, the stretching properties of fluid elements and vorticity along Lagrangian paths are studied in a channel flow at $\mathrm{Re}_\tau = 1000$ and compared with prior known results from isotropic turbulence. To track Lagrangian paths in a public database containing direct numerical simulation results, the task-parallel algorithm previously employed in the isotropic database is extended to the case of flow in a bounded domain. It is shown that above 100 viscous units from the wall, stretching statistics are equal to their isotropic values, in support of the local isotropy hypothesis. In the viscous sublayer, these stretching statistics approach values more consistent with an unsteady two-dimensional shear flow, in which exponential stretching no longer occurs. Normalized by dissipation rate, the stretching in the buffer layer and below is less efficient due to less favorable alignment statistics. The Cramér function characterizing cumulative Lagrangian stretching statistics shows that overall the channel flow has about half of the stretching per unit dissipation compared with isotropic turbulence.

DOI: 10.1103/PhysRevFluids.2.014605

I. INTRODUCTION

Along Lagrangian trajectories in turbulence, the velocity gradient tensor determines the deformation and rotation of infinitesimal fluid elements as well as the stretching and tilting of vorticity. These two processes are mathematically similar for an inviscid flow [1], but key differences exist for finite viscosity [2], such as the viscous tilting effect on vorticity [3]. The statistical properties of turbulent fluid deformation and vorticity stretching have been primarily studied in the context of homogeneous isotropic turbulence [3–14].

Because velocity gradients are dominated by contributions of small-scale motions near the Kolmogorov length scale ($\eta = \nu^{3/4}\langle\epsilon\rangle^{-1/4}$, where ν is the kinematic viscosity and $\langle\epsilon\rangle$ is the dissipation rate per unit mass), Kolmogorov's hypotheses [15] imply (approximately) universal isotropic behavior for velocity gradients at high Reynolds numbers far enough from solid boundaries, even for very anisotropic turbulent flows. The refined similarity hypothesis [16,17] further implies (possible) dependence on the local Reynolds number, i.e., intermittency effects. It follows from these hypotheses that the statistics of fluid deformation and vorticity stretching in regions of turbulent flows with high enough local Reynolds number and far enough from solid boundaries should be similar to those of isotropic turbulence, which have been studied in some detail. It is of interest, therefore, to investigate the details of material deformation and vorticity stretching in anisotropic

*pjohns86@jhu.edu

flows with solid boundaries. For instance, it is interesting to investigate the extent to which locally isotropic behavior can be observed in stretching statistics at locations far enough from the wall and how such statistics deviate from local isotropy near the wall.

In addition to the statistics of material deformation and vorticity stretching rates at a particular instant in time, it is also important to consider the statistics of cumulative deformation along Lagrangian paths, i.e., finite-time Lyapunov exponents (FTLEs). In the long-time limit, such cumulative statistics are expected to have a large-deviation principle [18], so the long-time behavior of the probability density functions (PDFs) may be summarized by a Cramér function [7,12,13,19]. Investigation along these lines may provide insight for a wide range of phenomena in wall-bounded flows including polymer-induced drag reduction [19–21], the kinematics of Lagrangian coherent structures [22–24], and the deformation of immiscible droplets and bubbles [10,11,25].

The Johns Hopkins Turbulence Database (JHTDB) provides a platform for on-demand tracking of Lagrangian particles through time-resolved Eulerian databases with snapshots from direct numerical simulation (DNS) results [26]. While the tracking of Lagrangian or inertial particles can be done at run-time inside the DNS code and stored in a Lagrangian database (e.g., [27]), the Eulerian database approach provides benefits such as flexibility to define seeding locations without needing to rerun the simulation or the ability to interrogate other flow variables such as the pressure Hessian along trajectories, as well as the ability to track particles backward in time [28]. Various algorithms for computing large ensembles of Lagrangian trajectories within the parallel database architecture of JHTDB have been studied, with a task-parallel approach providing the best overall performance [29]. In this work we extend the task-parallel approach to track Lagrangian particles in a bounded domain, namely, the $\mathrm{Re}_\tau = 1000$ channel flow DNS database [30].

The paper is organized as follows. First, the relevant mathematical background for quantifying the statistics of velocity gradients, material deformation, and vortex stretching is summarized in Sec. II. Then, Sec. III introduces the channel and isotropic DNS data sets used in the analysis and briefly details the development of the task-parallel Lagrangian tracking algorithm for the channel database. Analysis results are given in Sec. IV for instantaneous statistics as a function of wall distance as well as cumulative statistics for the whole channel. When possible, comparison is made with statistics from isotropic turbulence to highlight similarities and differences. A summary and conclusions are provided in Sec. V.

II. BACKGROUND

A. Velocity gradient statistics in channel flow

In a turbulent channel flow, the statistics are only nonhomogeneous in the wall-normal direction. Kinetic energy is dissipated by both the mean flow and turbulent fluctuations: $\langle\epsilon\rangle(y) = 2\nu(\langle S_{ij}\rangle\langle S_{ij}\rangle + \langle S'_{ij}S'_{ij}\rangle)$, where angular brackets denote ensemble averaging and S_{ij} is the strain-rate tensor. However, energy dissipation by the mean flow becomes negligible for $y^+ \gg 1$, i.e., in the logarithmic layer and core of the channel. At a given friction Reynolds number, the scale separation between large energetic motions and small dissipative motions increases with wall distance [31]. The typical magnitude of turbulent velocity gradients at a given distance from the wall is characterized by the Kolmogorov time scale

$$\tau'_\eta(y) = \sqrt{\frac{\nu}{\langle\epsilon\rangle_{\mathrm{turb}}}} = \frac{1}{\sqrt{2\langle S'_{ij}S'_{ij}\rangle}}. \tag{1}$$

For a typical magnitude of total velocity gradients (mean plus fluctuating), the Kolmogorov time scale can be generalized to include the mean strain rate

$$\tau_\eta(y) = \sqrt{\frac{\nu}{\langle\epsilon\rangle}} = \frac{1}{\sqrt{2(\langle S_{ij}\rangle\langle S_{ij}\rangle + \langle S'_{ij}S'_{ij}\rangle)}}. \tag{2}$$

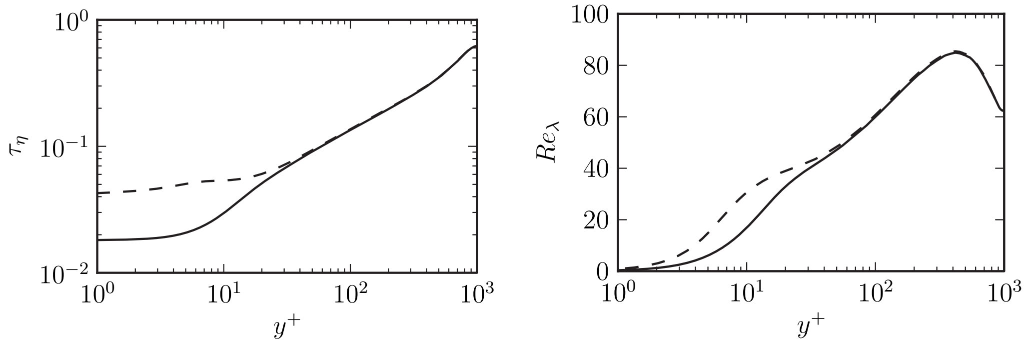

FIG. 1. Kolmogorov time scale (left) and Taylor-scale Reynolds number (right) as a function of distance from the wall. Dashed lines indicate values calculated with only turbulent dissipation, while solid lines indicate values using both turbulent and mean flow dissipation.

It will be argued that this more inclusive time scale is useful in the channel flow because the mean flow is also able to perform stretching in addition to the turbulent fluctuations, especially in the viscous sublayer and buffer region. Near the wall, i.e., $y^+ \sim 1$, this definition of Kolmogorov scale becomes $\tau_\eta \sim \tau_{\text{viscous}}$, where $\tau_{\text{viscous}} = \frac{\nu}{u_*^2}$ is the viscous time scale, while it equals the traditional Kolmogorov time scale when the mean strain rate becomes negligible (i.e., at $y^+ \gg 1$). Assuming an approximate balance between production and dissipation in the logarithmic region, where $-\langle u'v'\rangle \approx u_*^2$ and $\frac{\partial \langle u\rangle}{dy} \approx \frac{u_*}{\kappa y}$, then $\tau_\eta(y) \sim \sqrt{y^+}\tau_{\text{viscous}}$. At the centerline of the channel, the mean strain rate exactly vanishes and dissipation is done only by the turbulent fluctuations. Extrapolating the scaling law from the logarithmic region, the time scale at the center of the channel is $\tau_{\eta,c} \sim \text{Re}_\tau^{1/2}\tau_{\text{viscous}}$. For the remainder of this paper, we refer to this generalized Kolmogorov time scale simply as the Kolmogorov time scale.

To quantify the average strain-rate magnitude available over the whole channel, a bulk Kolmogorov time scale can be defined according to

$$\tau_{\eta,\text{bulk}} = \sqrt{\frac{2h\nu}{\mathcal{E}}}, \quad \mathcal{E} = \int_{-h}^{h} \langle \epsilon \rangle dy. \tag{3}$$

This time scale has a physical basis, since $\rho\mathcal{E} = -\frac{\dot{m}}{\rho}\frac{dp}{dx}$ represents the pumping power needed to force the channel flow at mass flow rate $\dot{m} = \rho\int_{-h}^{h}\langle u_1\rangle dy = 2h\rho U_{\text{bulk}}$. We thus can write $\tau_{\eta,\text{bulk}} = \sqrt{\frac{h\nu}{u_*^2 U_{\text{bulk}}}} = (\frac{1}{2}C_f)^{1/4}\text{Re}_\tau^{1/2}\tau_{\text{viscous}}$.

The separation of scales between large-scale (more flow dependent) and small-scale (more universal) turbulent motions is quantified in isotropic turbulence by the Taylor-scale Reynolds number $\text{Re}_\lambda = \frac{\sqrt{\langle u_1'^2\rangle}}{\nu\sqrt{|f''(0)|}}$, where $f(r) = \langle u_1'(\mathbf{x})u_1'(\mathbf{x}+r\mathbf{e}_1)\rangle/\langle u_1'^2\rangle$ is the longitudinal correlation function. For the channel flow, it is useful to characterize the separation of scales at a given height from the wall, which can be accomplished using the Taylor-scale Reynolds number expressed in terms of kinetic energy and mean dissipation rate

$$\text{Re}_\lambda(y) = \frac{2\sqrt{15}}{3}\frac{k}{\sqrt{\nu\langle\epsilon\rangle}}, \tag{4}$$

where $k(y) = \frac{1}{2}\langle u_i'u_i'\rangle$ is the turbulent kinetic energy at a given wall distance.

Figure 1 shows the generalized Kolmogorov time scale and Taylor-scale Reynolds number as a function of wall distance as computed from the JHTDB channel flow data set at $\text{Re}_\tau = 1000$ (details in Sec. III). In both panels, the values are alternatively calculated using only the dissipation of turbulent fluctuations, i.e., without the mean flow dissipation, and plotted as a dashed line. Above $y^+ \approx 50$, the difference between the two is negligible, signaling that practically all the dissipation is accomplished by the turbulent fluctuations (mean strain rate is negligible).

The Kolmogorov time scale is plotted on a log-log scale and displays an approximate power-law region where $\tau_\eta \sim y^n$, where $n \sim 0.5$, close to the theoretical prediction assuming local balance between production and dissipation of kinetic energy. The velocity gradient magnitudes ($\sim\tau_\eta^{-1}$) are highest near the wall and decay monotonically to the lowest magnitudes at the center of the channel ($y^+ = 1000$). With highest fluid deformation rates occurring nearest the wall, we may naively expect the Lyapunov exponents to be largest in magnitude nearest the wall as well, something that will be checked in Sec. IV.

In the fully turbulent region of the channel flow ($y^+ > 50$), the Taylor-scale Reynolds number is between 50 and 90. The peak Reynolds number occurs near $y^+ = 400$ rather than at the center of the channel. In this light, there is only moderate scale separation in the fully turbulent region. With such moderate Reynolds numbers, it is of interest to compare stretching statistics in the fully turbulent region of the channel to those of isotropic turbulence, i.e., to test the hypothesis of local isotropy in the context of stretching statistics. Approaching the wall, Re_λ vanishes due to vanishing turbulent kinetic energy.

B. Finite-time Lyapunov exponents

While the strain rate S_{ij} gives the instantaneous rate of fluid deformation, the *cumulative* deformation of fluid particles is described by the finite-time Lyapunov exponents of the Lagrangian map $\mathcal{T}_{t_0,t} : \mathbf{X} \in \mathbb{R}^3 \mapsto \mathbf{x} \in \mathbb{R}^3$ from an initial position $\mathbf{X}$ at time t_0 to a position $\mathbf{x}$ at a later time t. The Lagrangian map evolves as $\frac{dx_i}{dt} = u_i(\mathbf{x}(t),t)$ with initial condition $x_i(t_0) = X_i$. The geometry of an infinitesimal fluid element centered at $\mathbf{x}(t)$ can be described by the deformation tensor $D_{ij} = \partial x_i/\partial X_j$, which is the sensitivity of the trajectory to initial position. The evolution equation for the deformation tensor is

$$\frac{dD_{ij}}{dt} = A_{ik}D_{kj}, \tag{5}$$

with initial condition $D_{ij}(t_0) = \delta_{ij}$, where d/dt denotes Lagrangian (material) derivative.

A singular value decomposition (SVD) of the deformation tensor $D_{ij} = U_{ik}\Sigma_{k\ell}V_{j\ell}$ is useful for separating the deformation tensor into its magnitude (represented by the diagonal matrix Σ) and direction (columns of the unitary matrix $\mathbf{U}$). This is equivalent to an eigenvalue decomposition of the (left) Cauchy-Green tensor $C_{ij} = D_{ik}D_{jk} = U_{ik}\Sigma^2_{k\ell}U_{j\ell}$. The singular values σ_i give the ratio fluid stretching along its associated Lyapunov vector, thus by definition $\sigma_i(t_0) = 1$. In an incompressible flow, the volume of the fluid element must be preserved, i.e., $\sigma_1\sigma_2\sigma_3 = 1$ for all t. The singular value decomposition of (5) results in evolution equations for the singular values and their associated (forward) singular vectors [32]

$$\frac{d\ln\sigma_i}{dt} = \widehat{S}_{(ii)}, \quad U_{ki}\frac{dU_{kj}}{dt} = \begin{cases} \left(\frac{1+\frac{\sigma_j}{\sigma_i}}{1-\frac{\sigma_j}{\sigma_i}}\right)\widehat{S}_{ij} + \widehat{\Omega}_{ij}, & i \neq j \\ 0, & i = j, \end{cases} \tag{6}$$

where the caret denotes rotation to the Lyapunov reference frame, e.g., $\widehat{S}_{ij} = U_{ki}S_{k\ell}U_{\ell j}$. Repeated indices in parentheses are not summed. The singular values grow exponentially in time according to $\widehat{S}_{(ii)}$, i.e., the longitudinal velocity gradient along the direction of the ith singular vector. For this reason, we refer to $\widehat{S}_{(ii)}$ as an instantaneous Lyapunov exponent (ILE).

Finite-time Lyapunov exponents measure the time-averaged rate of exponential growth of each singular value over a certain interval along a Lagrangian path (i.e., exponential stretching along the direction of the associated singular vector)

$$\gamma_i(T;\mathbf{X},t_0) = \frac{1}{T}\ln\sigma_i(t_0+T;\mathbf{X},t_0) = \frac{1}{T}\int_{t_0}^{t_0+T}\widehat{S}_{(ii)}(\mathbf{x}(t'),t')dt', \tag{7}$$

where $T = t - t_0$ is the time interval over which the cumulative stretching is observed. Assuming ergodicity in homogeneous flows, the FTLEs converge for $T \to \infty$ to the Lyapunov exponents $\lambda_i = \langle\widehat{S}_{(ii)}\rangle = \langle\gamma_i\rangle$, with probability one. Similarly in this limit, the singular vectors of the deformation tensor (eigenvectors of the left Cauchy-Green tensor) converge to the Lyapunov vectors. The statistical alignment of Lyapunov vectors and strain-rate eigenvectors plays a key role in determining cumulative fluid particle deformation along with the strain-rate eigenvalues themselves Λ_i. For instance, in the eigenframe of the strain-rate tensor $\widehat{S}_{(ii)} = \cos^2(\theta_{ij})\Lambda_j$, where θ_{ij} is the angle between the ith eigenvector of the Cauchy-Green tensor and the jth eigenvector of the strain-rate tensor. In a channel flow, the Lyapunov exponents and other statistics involving finite-time Lyapunov exponents naturally depend on wall distance.

C. Vorticity stretching

The vorticity along a Lagrangian path evolves according to a very similar equation as fluid deformation, but with an added viscous term

$$\frac{d\omega_i}{dt} = A_{ij}\omega_j + \nu\nabla^2\omega_i. \tag{8}$$

Since vorticity is a vector (not tensor) quantity, a simple decomposition into magnitude and unit vector $\omega_i = \omega\widehat{\omega}_i$ takes the role of the SVD above. Decomposing (8), an evolution equation for the vorticity magnitude and direction is recovered [13],

$$\begin{aligned}\frac{d\ln\omega}{dt} &= \widehat{\omega}_i S_{ij}\widehat{\omega}_j + \nu\frac{\omega_i\nabla^2\omega_i}{\omega^2},\\ \frac{d\widehat{\omega}_i}{dt} &= (\delta_{ik} - \widehat{\omega}_i\widehat{\omega}_k)S_{kj}\widehat{\omega}_j + \nu\left[(\delta_{ik} - \widehat{\omega}_i\widehat{\omega}_k)\frac{\partial^2\widehat{\omega}_k}{\partial x_j\partial x_j} + 2\frac{\partial\widehat{\omega}_i}{\partial x_j}\frac{\partial\ln\omega}{\partial x_j}\right].\end{aligned} \tag{9}$$

Retaining the full equation for the vorticity alignment (i.e., strain rate and viscous tilting) but neglecting the role of viscosity in limiting the growth of vorticity, useful comparisons between vorticity stretching and fluid element deformation can be made [13]. An analog to the finite-time Lyapunov exponent can be constructed for cumulative vorticity stretching by considering only the inviscid part of vorticity stretching $\frac{d\ln\omega}{dt} = \widehat{\omega}_i S_{ij}\widehat{\omega}_j = \widehat{S}_\omega$, while retaining the viscous effects on vorticity realignment

$$\gamma_\omega(T;\mathbf{X},t_0) = \frac{1}{T}\ln\omega(t_0+T;\mathbf{X},t_0) = \frac{1}{T}\int_{t_0}^{t_0+T}\widehat{S}_\omega(\mathbf{x}(t'),t')dt. \tag{10}$$

Again, an ergodic assumption for homogeneous flows means that the $T \to \infty$ limit converges to an analog of the Lyapunov exponent for vorticity stretching $\lambda_\omega = \langle\widehat{S}_\omega\rangle = \langle\gamma_\omega\rangle$. As with fluid deformation, the alignment between vorticity and strain-rate eigenvectors plays a key role alongside strain-rate eigenvalue statistics in determining vorticity stretching statistics. For instance, the instantaneous vorticity stretching rate can be decomposed as $\widehat{S}_\omega = \cos^2(\theta_{\omega,j})\Lambda_j$, where $\theta_{\omega,j}$ represents the angle between the vorticity and the jth eigenvector of the strain-rate tensor. The instantaneous statistics of $\widehat{S}_\omega$ and $\widehat{S}_{(ii)}$ as well as their finite-time averages γ_ω and γ_i are useful for comparing vorticity stretching statistics with those of fluid element deformation. In the channel flow, ensemble averages of instantaneous stretching quantities vary with wall distance, meaning that the time-integrated Lagrangian stretching quantities will depend on the details of the past trajectory in moving closer to or farther from the wall.

D. Large-deviation statistics

In homogeneous isotropic turbulence, the PDFs of γ_i and γ_ω have been shown to follow a large-deviation principle $p_{\gamma_i}(g,T) \sim \exp[-T S_i(g)]$ for $T \to \infty$ [7,12,13]. When a large-deviation principle exists, the Cramér function $S_i(g)$ prescribes the self-similar form of the PDF as it collapses toward at Dirac δ function at λ_i. This has been useful for predicting power-law tails for polymer stretch lengths and the onset of significant polymer stretching for Oldroyd-B polymers [18,33] as well as droplet shape deformation statistics and the onset of droplet break-up for immiscible viscous droplets [11] in isotropic turbulence.

At sufficiently long integration times allowing for particles to mix thoroughly in the wall-normal direction, the lack of statistical homogeneity in this direction is not an obstacle for the existence of a large-deviation principle. Indeed, Bagheri *et al.* [19] showed for a channel flow with $\mathrm{Re}_\tau = 180$ that PDFs for γ_1 collapse self-similarly to a Cramér function that is independent of wall-normal location at the end of the trajectory. The predicted power-law PDFs for the polymer stretch were also observed.

An efficient method for simultaneously demonstrating the existence of a large-deviation principle and computing the Cramér function uses the scaled cumulant generating function (SCGF)

$$L_{\gamma_i}(q) = \lim_{T\to\infty} \frac{1}{T} \ln\langle \exp[q\gamma_i T]\rangle. \tag{11}$$

For fluid deformation, γ_i represents the finite-time Lyapunov exponents and $L(q)$ is sometimes called the generalized Lyapunov exponent [34]. According to the Gärtner-Ellis theorem [35,36], the existence of the limit in (11) is sufficient to prove the existence of a large-deviation principle for that quantity. The (convex hull of the) Cramér function can then be directly computed from the SCGF via Legendre transform

$$S_{\gamma_i}(g) = \sup_q [gq - L_{\gamma_i}(q)]. \tag{12}$$

Johnson and Meneveau [12] demonstrated that this method is more efficient than directly constructing the Cramér function via histograms.

III. NUMERICAL METHODS

In this section, the numerical methods used for this study are briefly summarized. Although this paper focuses mainly on channel flow results, frequent comparison with isotropic turbulence is made. Direct numerical simulation data for both channel flow and isotropic turbulence are obtained from the JHTDB. In order to obtain the necessary Lagrangian particle paths, the JHTDB Lagrangian tracking algorithm was extended to work in the channel flow data set. This extension is briefly summarized with discussion of particle tracking concerns unique to the channel data set.

A. Direct numerical simulation databases

This study makes use of both the channel flow and isotropic turbulence data sets from the JHTDB [37,38]. The isotropic data set was generated using a pseudospectral Navier-Stokes solver with low-wave-number forcing. The lowest two wave numbers in a $(2\pi)^3$ domain were forced in such a way as to keep their energy constant in time. A second-order Adams-Bashforth method was used for time advancement with $2\sqrt{2}/3$ truncation with phase shift used for dealiasing [39]. The numerical resolution is 1024^3 and the Taylor-scale Reynolds number is around $\mathrm{Re}_\lambda = 430$. The code wrote the full velocity and pressure field to disk every ten time steps for storage on the database. As a result, 1024 snapshots are stored with a database temporal resolution of $\Delta t_{\mathrm{db}} \approx \tau_\eta/22$, enough for a time sequence of $T_{\mathrm{db}} \approx 46\tau_\eta$. Table I summarizes the details of the isotropic simulation.

The channel flow data set was generated from a Navier-Stokes simulation using a pseudospectral method in the plane parallel to the walls and a seventh-order B splines collocation method in the

TABLE I. Numerical details for isotropic data-set simulation used in this paper [37].

N	Re_λ	ϵ	ν	η	τ_η	Δt	$k_{\max}\eta$
1024^3	433	0.093	1.85×10^{-4}	2.87×10^{-3}	0.045	2×10^{-4}	1.39

wall-normal direction [30,40]. For the simulation, the Navier-Stokes equations were formulated in wall-normal velocity-vorticity form [41]. Pressure was computed through solving the pressure Poisson equation only when writing to disk, which was every five time steps for 4000 snapshots, enough for about one domain flow-through time. The simulation domain size was $8\pi \times 2 \times 3\pi$ with a resolution of $2048 \times 512 \times 1536$ in the streamwise (x), wall-normal (y), and spanwise (z) directions, respectively. Time advancement was done with a third-order low-storage Runge-Kutta method and $2/3$ truncation was performed for dealiasing [42]. A constant pressure gradient was enforced to drive the flow at $\mathrm{Re}_\tau = 1000$ ($\mathrm{Re}_{\mathrm{bulk}} = \frac{2hU_{\mathrm{bulk}}}{\nu} = 40\,000$) with near unity bulk velocity. Table II includes further details about the channel flow simulation.

B. Lagrangian particle tracking

An important aspect of this study was the ability to compute Lagrangian trajectories from the Eulerian databases. This functionality was previously implemented in the JHTDB for the unbounded flows via the *getPosition* function, which uses a second-order predictor-corrector method for time advancement with user choice of fourth-, sixth-, and eighth-order Lagrangian interpolation in space and piecewise cubic Hermitian interpolation in time [26]. Kanov and Burns [29] developed an asynchronous task-parallel algorithm for improving the query response time. For this study, we extended the Lagrangian tracking capabilities to the channel data set with the task-parallel approach.

Initially, the *getPosition* function was implemented using a mediator synchronization approach (see Fig. 2). In this approach, a mediator (in this case the web server) accepts a batch of particle positions and determines which database contains their velocities. Upon completion of this task, the mediator spawns a process in each particle's respective database to advect each particle for the given integration step. Once complete, the new positions are returned to the mediator and the mediator must wait for all particles to complete for each integration step. After each step, the particles are reassigned to their new database location based on each particle's new position. This will be either the same database or a different one depending upon whether the particle crossed a database boundary. While this approach works, two other methods of particle tracing were experimented with, data-parallel and task-parallel methods.

The task-parallel method works differently from the mediator synchronization approach in that the mediator is not responsible for tracking each particle at every integration step. Instead, the mediator performs the initial placement of particles based on their respective positions in the database and then the database performs each integration step upon advecting each particle. This allows for the particle's computation to remain on the server in which the particle is placed. The only concern with this approach is when a particle crosses a server boundary; the original server is still responsible for follow-on integration steps. However, during testing this issue did not outweigh the speed gained from allowing each particle to advance asynchronously at each integration, thus making this the preferred approach.

TABLE II. Numerical details for the channel flow data set used in this paper [30].

N_x	N_y	N_z	Re_τ	dp/dx	ν	u_*	U_{bulk}	Δx^+	Δz^+	Δt
2048	512	1536	1000	-2.5×10^{-3}	5×10^{-5}	5×10^{-2}	1.00	12.3	6.1	1.3×10^{-3}

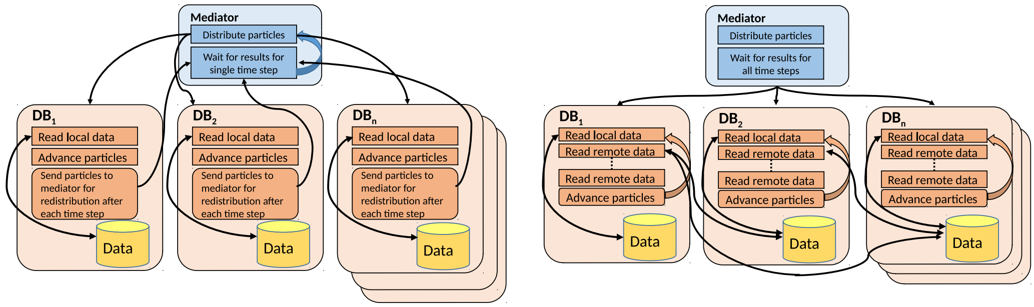

FIG. 2. Schematic showing the mediator synchronization and task-parallel algorithms for parallel processing of Lagrangian trajectories in the JHTDB. Mediator synchronization is on the left and the task-parallel algorithm is on the right.

Because the simulation was computed and stored in the database on a moving grid with velocity 0.45 in the streamwise direction, this had to be taken into account within the particle tracking calculation. At the beginning of a *getPosition* query, $0.45t_{\mathrm{start}}$ is subtracted from the physical x position of the particle, moving it from the physical location to the grid location. Then, throughout the particle tracking calculation, 0.45 is subtracted from the streamwise velocity component. Finally, at the conclusion of the calculation, $0.45t_{\mathrm{end}}$ is added back to the grid position to recover the physical position of the particle. Periodic wrapping in x and z is used to keep the particle always somewhere in the domain.

One additional consideration when implementing the Lagrangian path procedure in the channel data set was the numerical (but not physical) possibility that Lagrangian particles could travel through the walls at $y = \pm 1$. If the particles moves outside the domain ($|y| > 1$) during the predictor phase, then zero velocity is applied for the corrector step and hence half of the predictor velocity is used when actually advancing the particle. In this way, for a particle at distance y from the wall, the maximum time step allowed for which the particle remains in the domain is $\Delta t_{\max} = \frac{2y}{v(y)}$, where $v(y)$ is the wall-normal velocity from the predictor step (possibly the result of interpolation). In order to determine the maximum time step that can be taken with such a scheme without worrying about particles violating the no-penetration condition, the database was scanned to obtain the maximum velocity toward the wall at each y grid location.

The results are shown in Fig. 3. Using every 100th time step, each grid location was tested up to $y^+ = 30$. To find the minimum time step at which a particle could leave the domain, the range of y^+ values searched was narrowed and every tenth time step was searched. Finally, the minimum wall-normal location from this result was searched over the entire database. The result is that the minimum time step at which a particle could pass through the wall was found to be four times the

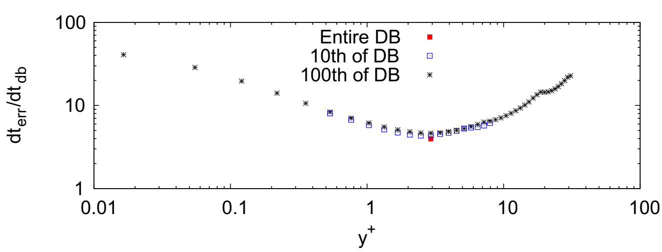

FIG. 3. Minimum time step, as a function of wall distance, at which a particle in the database (DB) may leave the domain by violating the no-penetration condition. The worst-case scenario is a particle leaving the domain from $y^+ \approx 3$ with a time step of $\Delta t = 2.6 \times 10^{-2}$, which is four times the database storage time step.

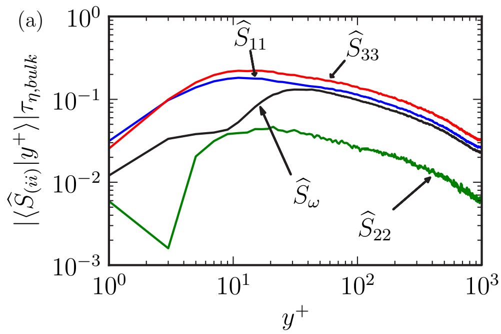

FIG. 4. Average instantaneous Lyapunov exponents $\langle\widehat{S}_{(ii)}\rangle$, for $i = 1,2,3,\omega$, as a function of wall distance (solid lines), (a) normalized by the bulk Kolmogorov time scale and (b) normalized by the local Kolmogorov time scale, with dashed lines representing $|\lambda_i|\tau_\eta$ from homogeneous isotropic turbulence.

database storage time step and 20 times the simulation time step. It is recommended that a time step at least as small as the storage time step be used, therefore, the current numerical method is deemed sufficient for preventing particles from violating the nonpenetration condition at the wall.

For the results in this study, ensembles of 43 200 particles were advanced through the entire database time with sixth-order spatial interpolation and a time step of $\Delta t = 0.0013$, i.e., the simulation time step. For initialization, the domain was split into 432 subdomains of size $\frac{\pi}{3} \times 1 \times \frac{\pi}{3}$. In each subdomain 100 particles were placed randomly according to a uniform distribution. Every five particle time steps (each database storage time step), the velocity gradient was retrieved from the database using fourth-order finite differencing and fourth-order Lagrangian interpolation in space. Johnson and Meneveau [12] explored the effect of simulation resolution as well as finite differencing on stretching statistics in isotropic turbulence, finding that low-order statistical quantities can be accurately obtained with the resolution and finite differencing used here in both channel and isotropic data sets.

IV. RESULTS

In this section, the DNS results concerning the statistics of material deformation and vorticity stretching in a channel flow at $\mathrm{Re}_\tau = 1000$ are explored. Comparisons with isotropic turbulence at $\mathrm{Re}_\lambda = 430$ are used when applicable. In addition to exploring the dependence of Lyapunov exponents on wall distance, the factors contributing to these trends, such as strain-rate eigenvalues and alignment between Cauchy-Green and strain-rate eigenvectors, are shown to provide additional insight.

A. Local Lyapunov exponents

Statistics of FTLEs can be difficult to obtain in a localized manner, since they naturally require integration over trajectories that move toward and away from the wall. Nonetheless, the mean of FTLE distributions can be easily localized to a particular y^+ location by averaging ILEs conditioned on wall distance. In this way, the local Lyapunov exponents (LLEs) $\langle\widehat{S}_{(ii)}|y\rangle$ represent the average stretching rates undergone by a material element (or vorticity) given that the current location of its trajectory is at that wall distance.

In order to characterize the mean stretching of material elements and vorticity as a function of wall distance, Fig. 4 presents LLEs normalized by bulk and local Kolmogorov time scales. In Fig. 4(a) the LLEs are normalized by the bulk Kolmogorov time scale, which is constant across the channel. The LLE magnitudes are plotted so that all results fit on a log-log plot. For most of the channel only $\langle\widehat{S}_{33}|y\rangle$ is negative, while all others are positive. The instantaneous stretching of

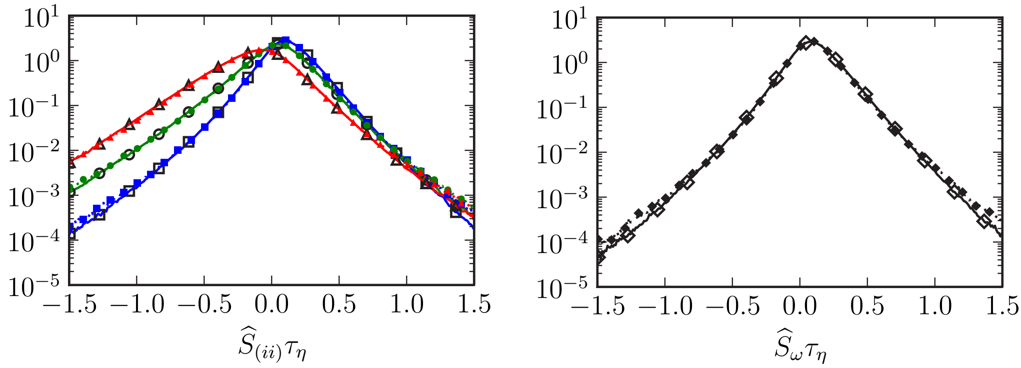

FIG. 5. PDFs of instantaneous Lyapunov exponents normalized by the local Kolmogorov time scale in the core of the channel, i.e., conditioned on $y^+ > 100$. Solid lines with open symbols represent channel flow results, while dotted lines with closed symbols represent isotropic turbulence results. Squares (left) show $\widehat{S}_{11}$, circles (left) $\widehat{S}_{22}$, triangles (left) $\widehat{S}_{33}$, and diamonds (right) $\widehat{S}_\omega$.

the maximal singular value $\langle \widehat{S}_{11}|y\rangle$ has a peak between $10 \leqslant y^+ \leqslant 20$, signifying that the maximum stretching of material lines occurs in the buffer layer, on average. The other two Lyapunov exponents $\langle \widehat{S}_{22}|y\rangle$ and $\langle \widehat{S}_{33}|y\rangle$ likewise have peak magnitudes in the buffer layer. The vorticity stretching LLE $\langle \widehat{S}_\omega|y\rangle$ has its peak further from the wall, near $30 \leqslant y^+ \leqslant 50$. This occurs because, while vorticity stretching is close in magnitude to material line stretching throughout the channel, it drops off more quickly approaching the wall through the buffer layer. The value of $\langle \widehat{S}_{22}|y\rangle$, meanwhile, drops off precipitously approaching the wall in the viscous sublayer and even becomes slightly negative below $y^+ = 3$, indicating that material deformation becomes mostly two dimensional.

Figure 4(b) normalizes the local Lyapunov exponents using the local Kolmogorov time scale, which increases monotonically with wall distance (see Fig. 1). By rescaling with local strain rate averages, the Lyapunov exponent represents something like an efficiency of stretching accomplished per unit available strain rate (dissipation). This allows direct comparison with isotropic turbulence, indicated by dashed lines in Fig. 4(b). For $y^+ > 100$, there is excellent agreement between the Lyapunov exponents of channel flow and isotropic turbulence. This shows that, above 100 viscous units from the wall, the variation of LLEs (including for vorticity stretching) with wall distance can be accurately predicted from Kolmogorov's hypothesis of local isotropy, given knowledge only of the y dependence of the Kolmogorov time scale, even though the Re_λ is not large.

Seeing from Fig. 4(b) that the LLE values are constant above $y^+ = 100$ when normalized by the local Kolmogorov time scale and equal to the values in isotropic turbulence, it is of interest to compare the entire distribution of $\widehat{S}_{(ii)}\tau_\eta$. Figure 5 shows the PDF of $\widehat{S}_{(ii)}\tau_\eta$ created from histograms binned along Lagrangian trajectories according to the Kolmogorov time scale of the current wall distance. The result is compared to the PDF of instantaneous Lyapunov exponents in homogeneous isotropic turbulence (dotted lines). It is immediately clear that the entire distributions are quite similar. The isotropic flow does have a higher Re_λ, thus is expected to have higher intermittency in velocity derivative statistics, which is evidenced by slightly wider tails for the isotropic data in Fig. 5. Grid resolution is another factor to consider when comparing the tails of these distributions, however, as Johnson and Meneveau [12] showed that resolution and finite differencing can significantly influence the statistics of larger fluctuations in fluid stretching. Nonetheless, comparing the cores of these distributions, this figure represents more detailed evidence that the local isotropy hypothesis is sufficient for describing the material deformation and vorticity stretching statistics above $y^+ = 100$.

Returning to Fig. 4(b), the stretching efficiency per unit dissipation $\langle \widehat{S}_{(ii)}|y\rangle\tau_\eta$ drops significantly approaching the wall. Near the wall, the combination of decreasing stretching efficiency per unit dissipation with increasing available dissipation causes the maximal stretching $\langle \widehat{S}_{(ii)}|y\rangle\tau_{\eta,\mathrm{bulk}}$ to occur in the buffer layer in Fig. 4(a). In order to explore the causes of this loss in stretching efficiency near the wall, it is useful to employ the following decomposition:

$$\widehat{S}_{(ii)} = \sum_{j=1}^{3} \Lambda_j \cos^2 \theta_{ij}, \tag{13}$$

which is obtained by taking the eigenframe of the strain-rate tensor, where Λ_j represents the jth eigenvalue of the strain-rate tensor and θ_{ij} represents the angle between the eigenvector of the Cauchy-Green tensor associated with its ith eigenvalue and the strain-rate eigenvector associated with its jth eigenvalue. Here eigenvalues are sorted in decreasing order. Note that we can also take $i = \omega$, where $\theta_{\omega j}$ then indicates angles between the vorticity vector and strain-rate eigenvectors. From this decomposition, it is clear that statistics of the ILEs at each wall-normal location are a function jointly of strain-rate eigenvalue statistics and alignment statistics. That is, the Lyapunov exponent can be written as

$$\langle \widehat{S}_{(ii)} | y \rangle = \sum_{j=1}^{3} \langle \Lambda_j \cos^2 \theta_{ij} | y \rangle. \tag{14}$$

Although statistical independence of Λ_j and θ_{ij} is neither expected nor observed, thus $\langle \Lambda_j \cos^2 \theta_{ij} | y \rangle \neq \langle \Lambda_j | y \rangle \langle \cos^2 \theta_{ij} | y \rangle$, it is nonetheless instructive to explore $\langle \Lambda_j | y \rangle$ and $\langle \cos^2 \theta_{ij} | y \rangle$ separately as a function of wall distance. Partly justifying this separation, it was found that correlation coefficients between the strain-rate eigenvalues and alignment angles were quite small, $\sim \pm\, 0.1$.

B. Strain-rate eigenvalues

The first ingredient in fluid element deformation and vorticity stretching statistics is the strain-rate magnitude statistics, characterized most effectively by its eigenvalues. It is first worth noting that by definition, at every wall-normal location,

$$\sum_{i=1}^{3} \langle \Lambda_i^2 | y \rangle \tau_\eta^2 = \frac{1}{2}. \tag{15}$$

Further, $\langle \Lambda_i^2 \rangle = \langle \Lambda_i \rangle^2 + \langle \Lambda'^2 \rangle$, so $\langle \Lambda_i \rangle^2 \leqslant \langle \Lambda_i^2 \rangle$, where equality holds only in the absence of fluctuations. Therefore, we conclude that

$$\sum_{i=1}^{3} (\langle \Lambda_i | y \rangle \tau_\eta)^2 \leqslant \frac{1}{2}. \tag{16}$$

Larger variance of Λ_i fluctuations tends to decrease the left-hand side.

Figure 6(a) shows the mean strain-rate eigenvalues as a function of wall distance, with constant-in-space normalization by $\tau_{\eta,\mathrm{bulk}}$. The maximal and minimal eigenvalues reach their peak magnitude at the wall, decreasing monotonically to the center of the channel. The intermediate eigenvalue, however, reaches its maximum in the buffer layer, since the flow in the viscous sublayer tends to resemble unsteady two-dimensional shear flow. The drop-off in Λ_2 near the wall is accompanied by equal magnitudes for Λ_1 and Λ_3 (opposite signs).

The mean strain-rate eigenvalues are rescaled with the local Kolmogorov time scale in Fig. 6(b). Here the dashed lines show the values from the isotropic data set. As with the Lyapunov exponent above, the mean strain-rate eigenvalues collapse to the isotropic values for $y^+ > 100$ when normalized this way. Thus, the hypothesis of local isotropy provides a good platform for describing the mean strain-rate eigenvalues' dependence on wall distance above 100 viscous units. The magnitude of the minimal strain-rate eigenvalue, which is always negative, remains approximately constant across the entire channel under this normalization. Meanwhile, the two-dimensional nature of the flow near the wall causes the intermediate strain-rate eigenvalue to vanish. To compensate,

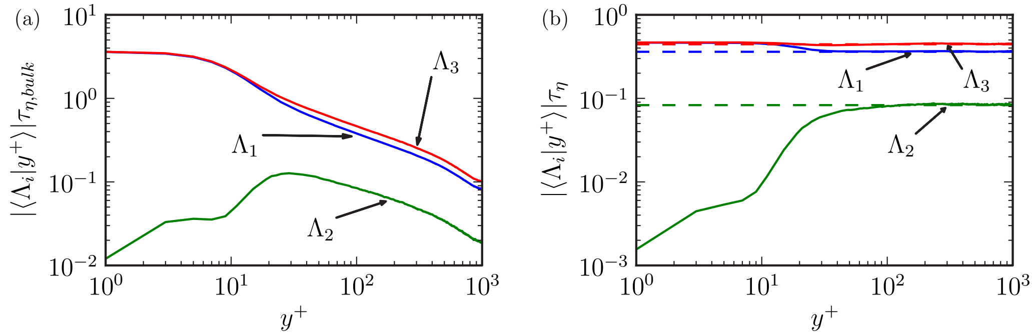

FIG. 6. Average strain-rate eigenvalues as a function of wall distance (solid lines), (a) normalized by the bulk Kolmogorov time scale and (b) normalized by the local Kolmogorov time scale, with dashed lines representing results from homogeneous isotropic turbulence.

the maximal strain-rate eigenvalue, which is always positive, increases in magnitude near the wall and becomes equal in magnitude to the minimal eigenvalue. The Kolmogorov time scale is an effective characterization of strain-rate magnitude available for deforming fluid elements or stretching vorticity. While alignment with the strain-rate eigenvector corresponding to its intermediate eigenvalue is beneficial for stretching over most of the channel (i.e., because $\lambda_2 > 0$), near the wall such alignment provides very little stretching.

Since Fig. 6(b) shows that the mean strain-rate eigenvalues are constant for $y^+ > 100$, it is of interest to pursue the entire PDF of strain-rate eigenvalues in this region when normalized by the local Kolmogorov time scale. The resulting distribution (solid lines) is compared with the strain-rate eigenvalue PDFs from isotropic turbulence (dotted lines) in Fig. 7. The comparison is quite good, although the PDFs from the isotropic simulation have slightly wider tails due to their higher Re_λ. Therefore, the hypothesis of local isotropy for strain-rate eigenvalue statistics gains further support.

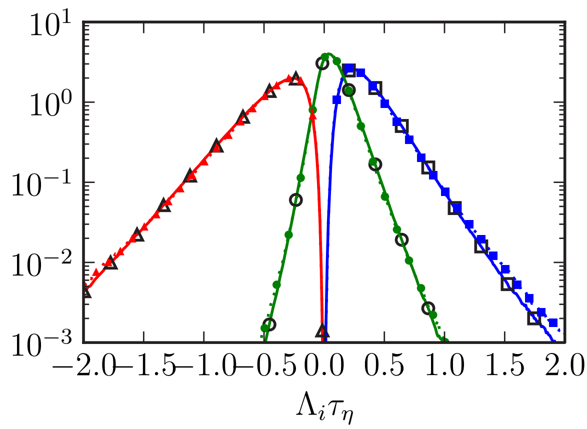

FIG. 7. PDFs of strain-rate eigenvalues normalized by the local Kolmogorov time scale in the core of the channel (solid lines with open symbols), i.e., conditioned on $y^+ > 100$. Dotted lines with closed symbols represent results from homogeneous isotropic turbulence. Squares show Λ_1, circles Λ_2, and triangles Λ_3.

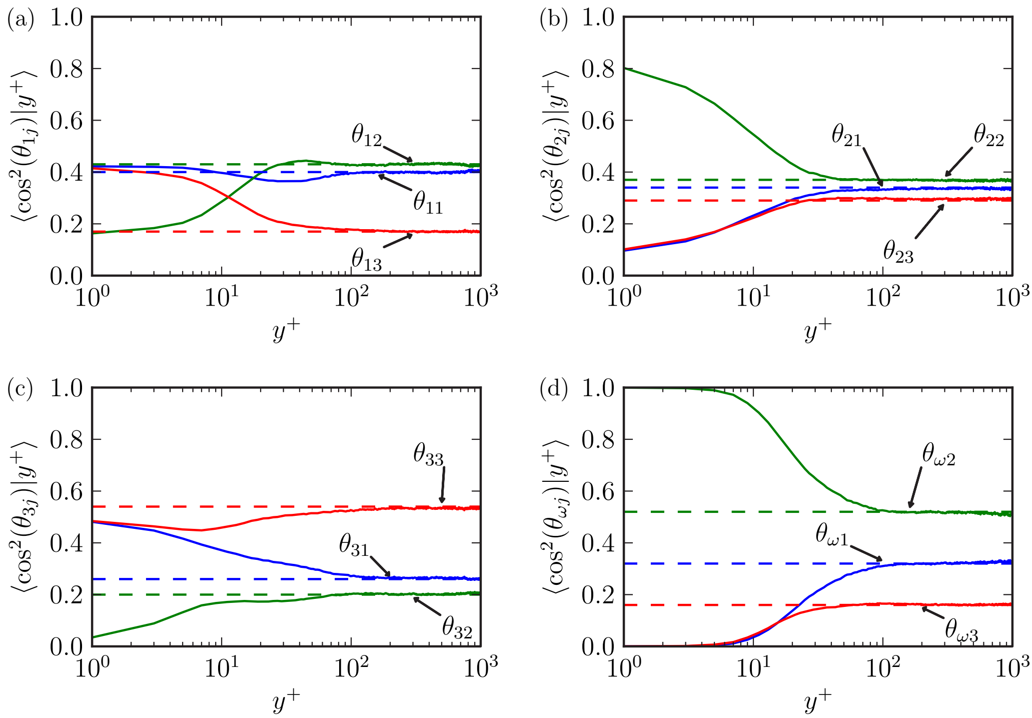

FIG. 8. Averages of $\cos^2(\theta_{ij})$ as a function of y^+, where θ_{ij} represents the angle between the Cauchy-Green eigenvector associated with its ith largest eigenvalue and the strain-rate eigenvector associated with its jth largest eigenvalue. Solid lines represent results for the (a) most extensive FTLE direction ($i = 1$), (b) intermediate FTLE direction ($i = 2$), (c) most compressive FTLE direction ($i = 3$), and (d) vorticity vector direction ($i = \omega$). Dashed lines represent results from homogeneous isotropic turbulence.

C. Alignment with strain-rate eigenvectors

The statistics of alignment between strain-rate eigenvectors and Cauchy-Green eigenvectors (or vorticity vectors) are of importance in determining the efficiency at which a turbulent flow stretches fluid elements (or vorticity) per unit dissipation. The average weights assigned to alignments between strain-rate and Cauchy-Green eigenvectors are given by $\langle\cos^2\theta_{ij}|y\rangle$, as discussed above. Figure 8 presents, as a function of wall distance, all the components of this tensor with $i = 1,2,3,\omega$ and $j = 1,2,3$.

The eigenvector associated with the largest eigenvalue of the Cauchy-Green tensor ($i = 1$) represents the asymptotic alignment direction of material lines. Its mean alignment with strain-rate eigenvectors for different wall distances in the channel flow is shown in Fig. 8(a) compared with isotropic turbulence alignments. As with previous observations in this paper, the mean alignment collapses to the isotropic values for $y^+ > 100$, indicating agreement with local isotropy assumptions. In the isotropic turbulence regime, the material line asymptotically aligns more closely with the strain-rate eigenvectors associated with the largest two eigenvalues, with slight preference for the intermediate eigenvalue. Meanwhile, it tends to align more orthogonally with the strain-rate eigenvector of the minimal eigenvalue (contracting direction). This bias in alignment allows for net stretching, since it experiences better alignment with the expanding eigenvectors than the contracting ones. The situation changes approaching the wall, however. Alignment with the largest strain-rate eigenvalue remains fairly steady, dipping slightly where $10 < y^+ < 100$ but rising above the isotropic value within ten viscous units of the wall. Alignment with the intermediate eigenvalue of the strain-rate tensor drops dramatically within 30 viscous units of the wall after a slight maximum where $30 < y^+ < 100$. The loss of alignment with the intermediate eigenvalue is replaced by more alignment with the contracting strain-rate eigenvalue. Approaching the wall, the alignment of material lines is equal with the Λ_1 and Λ_3 strain-rate eigenvectors. In this way, the stretching done by alignment with the expanding direction is statistically canceled by equal alignment and magnitude of the contracting direction. This increased alignment with the Λ_3 direction is the cause for the decreased mean stretching efficiency $\lambda_1\tau_\eta$ near the wall noticed in Fig. 4(b).

The mean alignments of the eigenvector for the intermediate Lyapunov exponent ($i = 2$) similarly collapse to isotropic values above $y^+ = 100$. This eigenvector shows the lowest level of bias in aligning with each of the three strain-rate eigenvectors, with a slight preference for the eigenvector of Λ_2 and against the eigenvector of Λ_3. Near the wall, however, it becomes strongly biased toward alignment with the Λ_2 eigenvalue, which is itself vanishing. Alignments with the Λ_1 and Λ_3 eigenvectors decrease significantly and become equal. The drop in $\lambda_2\tau_\eta$ near the wall in Fig. 4(b) is mostly a result of the drop in $\langle\Lambda_2\rangle$ due to the increasingly two-dimensional nature of the near wall flow.

The eigenvector of the minimal Lyapunov exponent ($i = 3$) also statistically mirrors the strain-rate eigenvalue alignments of isotropic turbulence for $y^+ > 100$. In this region, its preferential alignment with the contracting eigenvalue preserves the $\lambda_3 < 0$ relationship. Approaching the wall, however, this eigenvector's increasing alignment with the Λ_1 direction coupled with a slight decrease in alignment with Λ_3 effectively decreases the magnitude of $\lambda_3\tau_\eta$ as well, as seen in Fig. 4(b). The tendency toward contraction by Λ_3 becomes statistically canceled with more tendency toward stretching by Λ_1.

The vorticity vector shows the most exaggerated behavior, moving from its well-known alignment with the Λ_2 direction at $y^+ > 100$, toward the two-dimensional shear flow behavior in the viscous sublayer, where vorticity is perpendicular to the nonzero strain-rate eigenvalues. The drop-off in Λ_2 approaching the wall, along with the vorticity's dramatically increasing alignment with the Λ_2 direction, is responsible for the drop in vorticity stretching efficiency $\lambda_\omega\tau_\eta$ approaching the wall.

The following picture thus emerges. For $y^+ > 100$, alignment and strain-rate statistics mirror those of isotropic turbulence. In the viscous sublayer $y^+ < 5$, the flow becomes like an unsteady two-dimensional shear flow. In this regime, the Cauchy-Green tensor is relatively unstretched out of the shear plane (typically, the transverse direction). Thus, the λ_1 and λ_3 Cauchy-Green eigenvectors lie in the plane of the shear, while the vorticity is perpendicular to this plane. As a result, the vorticity directly opposes the efforts of the strain-rate tensor to tilt the λ_1 Cauchy-Green eigenvector toward the Λ_1 strain-rate eigenvector (and likewise λ_3 toward Λ_3). The stalemate that emerges results in statistically equal alignment of the λ_1 and λ_3 eigenvectors with stretching and contracting directions of the strain-rate tensor, which are approximately equal in magnitude. The λ_2 Cauchy-Green eigenvector aligns preferentially out of the shear plane (and with the vorticity vector) and thus experiences little stretching or contraction. In this limit, all three Lyapunov exponents effectively vanish and fluid elements are not stretched exponentially. In between these two limits, $5 < y^+ < 100$, the DNS results indicate a primarily monotonic interpolation in alignment statistics, though some nonmonotonic behavior is seen, for instance, in Fig. 8. Due to less optimal alignment statistics, buffer layer turbulence is evidently less efficient at material deformation and vorticity stretching compared with the locally isotropic turbulence seen at higher y^+, due to less favorable alignment statistics seen in that region. These alignment statistics, which are less favorable in the buffer layer compared to isotropic turbulence, could be due to the strong background shear (although not as influential as in the two-dimensional regime seen in the viscous layer) as well as the decrease in local Reynolds number and the increased influence of coherent structures on velocity gradient statistics. Of course, the strain-rate magnitudes in the buffer layer are much higher than in the core of the channel, so the maximal deformation and stretching still occur there.

Finally, Fig. 9 compares the full PDF of these alignments for $y^+ > 100$. As with the LLEs and strain-rate eigenvalues, its is true with the alignment statistics as well that the entire PDF matches

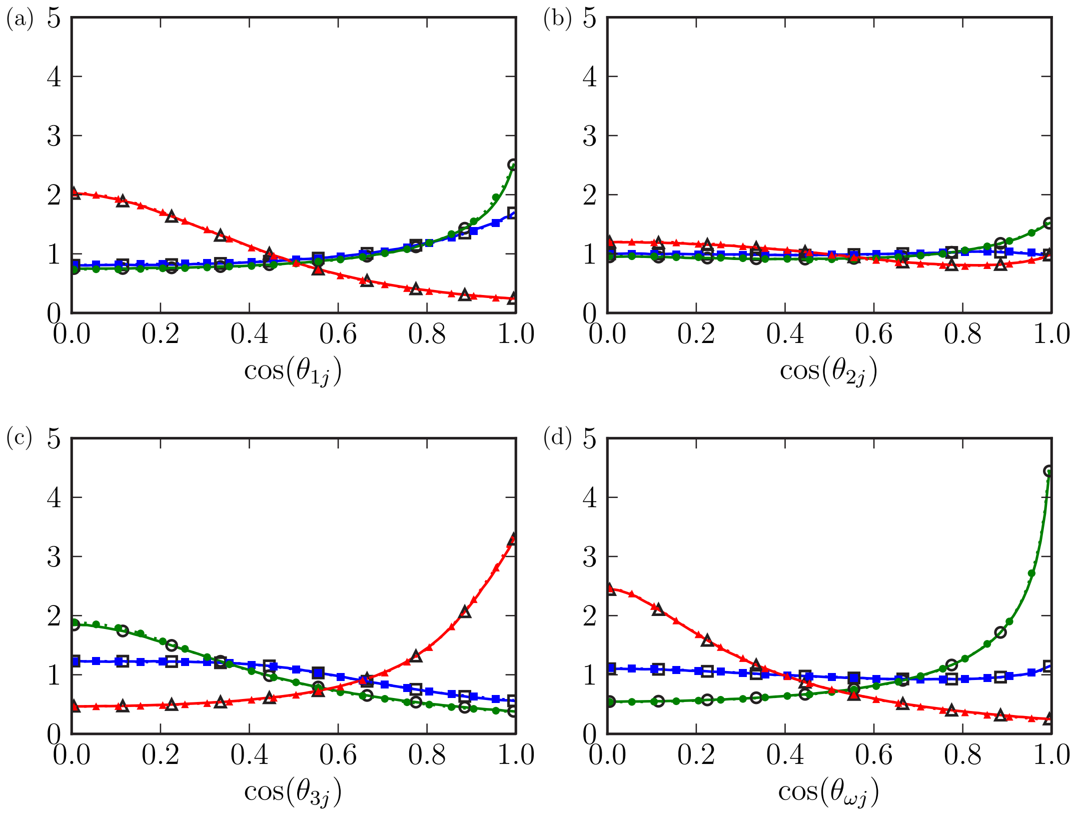

FIG. 9. PDFs of $\cos(\theta_{ij})$ in the core of the channel, i.e., conditioned on $y^+ > 100$. Solid lines represent the (a) most extensive FTLE direction ($i = 1$), (b) intermediate FTLE direction ($i = 2$), (c) most compressive FTLE direction ($i = 3$), and (d) vorticity unit vector. Dashed lines represent results from homogeneous isotropic turbulence. Squares show $j = 1$, circles $j = 2$, and triangles $j = 3$.

that of isotropic turbulence. In fact, many of the lines in Fig. 9 are indistinguishable. This figure completes the compelling evidence given in this paper that, above $y^+ = 100$, channel flow turbulence deforms fluid elements and stretches vorticity in a manner fully consistent with the hypothesis of local isotropy, even at relatively modest Reynolds numbers.

D. Cramér functions

For long integration time, assuming ergodic and mixing properties, the FTLEs along Lagrangian paths all converge to $\lim_{T\to\infty} \gamma_i(T) = \lambda_i$. The distribution of FTLEs in this limit collapses toward a Dirac δ function according to the self-similar shape dictated by the Cramér function $p_{\gamma_i}(g) \sim \exp[-T S_{\gamma_i}(g)]$. The Cramér functions for $i = 1,2,3,\omega$ are constructed using the Legendre transform of the SCGF introduced in Sec. II D. The SCGF $L_{\gamma_i}(q)$ is computed numerically via linear regression fit to $\ln\langle \exp(q\gamma_i T)\rangle$ as a function of T for different values of q. The derivative of the SCGF can also be calculated by a linear fit to $\frac{\langle \gamma_i T \exp(q\gamma_i T)\rangle}{\langle \exp(q\gamma_i T)\rangle}$. The Cramér function is then computed via a Legendre transform $S(g) = qL'(q) - L(q)$ with $g = L'(q)$.

Figure 10 presents the Cramér functions for the three FTLEs as well as for vorticity stretching in the channel flow (solid lines) compared with those of isotropic turbulence (dashed lines). Immediately evident is that the minima of the channel flow Cramér functions, which indicate the mean values λ_i, are closer to the origin than their isotropic counterparts. In fact, these mean values are tabulated

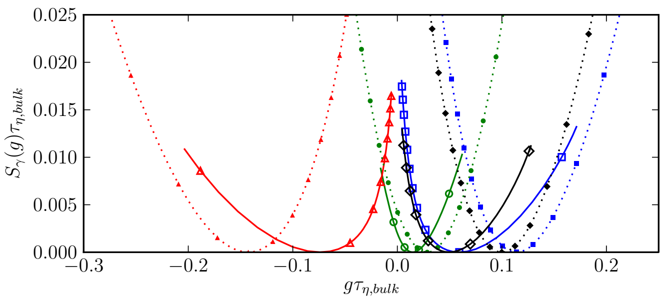

FIG. 10. Cramér functions of the three Lyapunov exponents and vorticity for the channel flow (solid lines with open symbols) compared to those from isotropic turbulence (dotted lines with closed symbols). Squares show γ_1, circles γ_2, triangles γ_3, and diamonds γ_ω.

in the first column of Table III. Each volume-averaged Lyapunov exponent, normalized by the volume-averaged dissipation rate, is approximately half as large as its counterpart from isotropic turbulence. The cumulative stretching accomplished by velocity gradients along Lagrangian paths in channel flow is less efficient per unit dissipation than is isotropic turbulence. While the turbulent stretching statistics are indistinguishable from those of isotropic turbulence in the core of the channel ($y^+ > 100$), it is clear that the alignment statistics in the buffer region and viscous sublayer are less favorable. As a result, in the locations of the highest available strain rates, the alignment efficiency drops dramatically below the values from isotropic turbulence. Nonetheless, the channel flow maintains approximately the same ratio between Lyapunov exponents because all are decreased proportionally.

The shape of the Cramér functions can be characterized by looking at the behavior of cumulants in the $T \to \infty$ limit [12]. Since the existence of the SCGF indicates the asymptotically linear growth of the cumulant generating function in time, the cumulants themselves likewise grow linearly. For instance, the variance of the FTLE distribution grows like $\Delta_i T$, where $\Delta_i = L''_{\gamma_i}(0)$ represents the width of the Cramér function. Furthermore, the third and fourth cumulants grow like $L'''(0)T$ and $L^{(4)}(0)T$, respectively, thus the skewness and excess kurtosis decrease in time as $\mathcal{S}_i = \frac{L'''_{\gamma_i}(0)}{L''_{\gamma_i}(0)^{3/2}\sqrt{T}}$ and $\mathcal{K}_i - 3 = \frac{L^{(4)}_{\gamma_i}(0)}{L''(0)^2 T}$, in accordance with the central limit theorem. These measures are summarized in Table III for both the channel flow and isotropic turbulence Cramér functions.

TABLE III. Minimum and width of the Cramér functions for channel flow and isotropic turbulence, along with coefficients for skewness and excess kurtosis (which decay as $T \to \infty$).

Channel	$\lambda_i \tau_\eta$	$\Delta_i \tau_\eta$	$\mathcal{S}_i\sqrt{\frac{T}{\tau_\eta}}$	$(\mathcal{K}_i - 3)(\frac{T}{\tau_\eta})$
$i = 1$	0.059	0.34	13.9	95
$i = 2$	0.014	0.07	10.9	263
$i = 3$	–0.073	0.53	–14.0	107
$i = \omega$	0.049	0.21	12.2	63
HIT	$\lambda_i \tau_\eta$	$\Delta_i \tau_\eta$	$\mathcal{S}_i\sqrt{\frac{T}{\tau_\eta}}$	$(\mathcal{K}_i - 3)(\frac{T}{\tau_\eta})$
$i = 1$	0.114	0.15	4.6	29
$i = 2$	0.029	0.10	0.9	3
$i = 3$	–0.143	0.26	–4.5	24
$i = \omega$	0.100	0.12	3.5	19

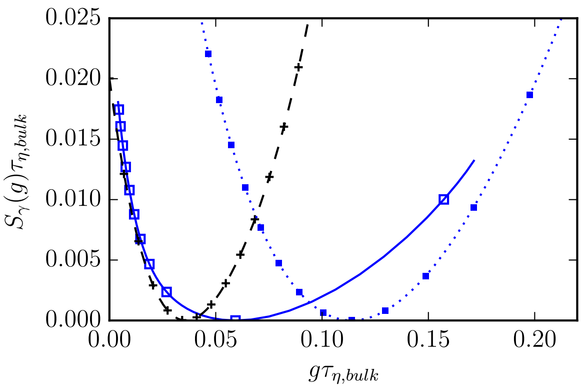

FIG. 11. Cramér function for the maximal finite-time Lyapunov exponent in a channel flow at $\mathrm{Re}_\tau = 180$ (dashed line with pluses, from [19]) and $\mathrm{Re}_\tau = 1000$ (solid lines with open symbols) compared to those from isotropic turbulence (dotted lines with closed symbols).

While the channel flow Cramér functions show a mean FTLE 50% below that of isotropic turbulence, the width of the Cramér functions for γ_1, γ_3, and γ_ω are about twice as large, indicating larger fluctuations in cumulative stretching. Furthermore, the channel flow displays much larger skewness and kurtosis values, with negative skewness for the negative FTLE and positive skewness for the positive ones. This statistical behavior reflects the influence of wall-normal movement of Lagrangian paths in causing the FTLEs to fluctuate more violently, particularly in creating rare events of large stretching and deformation when a particle advects into the high strain-rate region near the wall (and only occasionally will see beneficial alignments there). Such events appear not to cause as much fluctuation in γ_2, perhaps because they occur near the wall where the flow behaves more two dimensionally.

Finally, to briefly explore the influence of Re_τ, Fig. 11 compares the Cramér function for the maximal FTLE from the channel flow simulation of Bagheri *et al.* [19] at $\mathrm{Re}_\tau = 180$. Because they presented their results in terms of the time scale $\tau_L = h/U_{\mathrm{center}}$, their fourth-order polynomial fit to the Cramér function was carefully rescaled in terms of $\tau_{\eta,\mathrm{bulk}}$ using data from their paper. The mean stretching at $\mathrm{Re}_\tau = 180$ is $\lambda_1 \tau_{\eta,\mathrm{bulk}} = 0.036$, which is 30% of that seen in isotropic turbulence, even lower than the $\mathrm{Re}_\tau = 1000$ case. The width of the Cramér function (variance of FTLE fluctuations) is also much smaller for $\mathrm{Re}_\tau = 180$, which likely reflects the lower fluctuations due to wall-normal sweeping. As argued in Sec. II A, the range of strain-rate magnitudes in the channel flow scales as $\tau_{\eta,\mathrm{center}}/\tau_{\eta,\mathrm{wall}} \sim \mathrm{Re}_\tau^{1/2}$, meaning that the stretching can fluctuate more violently with increasing Reynolds number simply by wall-normal migration.

V. CONCLUSION

In this paper, the deformation of fluid elements and stretching of vorticity are explored in a channel flow at $\mathrm{Re}_\tau = 1000$ using both instantaneous and finite-time Lyapunov exponents. The Lagrangian paths are extracted from an Eulerian DNS database by adapting the task-parallel approach previously used for isotropic turbulence to the channel flow. It has been verified empirically based on the data that no particles can cross into the wall as long as an appropriate Lagrangian time step is used. When averaged conditionally on wall-normal location, the instantaneous Lyapunov exponents have a maximum in the buffer layer and approach zero at the wall. Their behavior for $y^+ > 100$ is dictated only by the local value of τ_η with magnitudes equal to those of homogeneous isotropic turbulence (equal stretching per unit dissipation). For $y^+ < 100$, however, the strain rate becomes less efficient than in isotropic turbulence in stretching fluid elements and vorticity, where alignments between Cauchy-Green and strain-rate eigenvalues become less favorable for sustained stretching. In this viscous sublayer, the alignment and stretching statistics betray the characteristics of two-dimensional unsteady shear flow, which is particularly poor at producing exponential stretching and deformation. In the buffer layer, the alignments are still less efficient for stretching than isotropic turbulence, though the flow topology is much more complex than in the viscous sublayer.

The probability density functions of instantaneous Lyapunov exponents, strain-rate eigenvalues, and alignments between Cauchy-Green and strain-rate eigenvalues all mimic those of isotropic turbulence when conditioned on $y^+ > 100$ and scaled according to the dissipation rate averaged conditionally on wall-normal location. Together, these provide strong support for the ability of the local isotropy hypothesis to describe quantities important in fluid element deformation and vorticity stretching in this region. The observed success of local isotropy is notable, since the large-scale fluctuations in the channel are highly anisotropic and the scale separation is relatively moderate ($\mathrm{Re}_\lambda \sim 80$) in the core. The contributions of strain rate and alignment statistics were explored separately in considering the departure from locally isotropic behavior near the wall.

The Cramér functions for finite-time Lyapunov exponents, describing cumulative deformation along Lagrangian paths, reflect the less efficient stretching near the wall when compared with those of isotropic turbulence. Per unit dissipation, the channel flow at $\mathrm{Re}_\tau = 1000$ provides about 50% of the stretching compared to isotropic turbulence, while ratios between the Lyapunov exponents remain about the same as in isotropic turbulence. This occurs because the maximum local stretching occurs in the buffer layer, where alignments between Cauchy-Green and strain-rate eigenvectors are not as propitious. The generation of large fluctuations in FTLEs by wall-normal movement of trajectories is reflected in increased Cramér function width, skewness, and excess kurtosis values compared to isotropic turbulence. An exception to this observation is γ_2, which actually tends to fluctuate less, perhaps due to its faster drop-off near the wall as the flow becomes more two dimensional.

While local isotropy is successful in describing the cumulative deformation behavior above $y^+ = 100$ and the viscous sublayer tends toward the behavior of unsteady two-dimensional shear flow, the intermediate behavior of the buffer layer is less straightforward. For instance, approaching the wall in the buffer layer, the mean vorticity stretching drops off sooner than the fluid element deformation. Description of this region is difficult because the influential anisotropic coherent structures are also responsible for dissipation and stretching.

ACKNOWLEDGMENTS

The authors thank Kalin Kanov for technical help with the JHTDB code base. P.L.J. was supported by a National Science Foundation Graduate Research Fellowship Program under Grant No. DGE-1232825 and C.M. by a National Science Foundation Grant No. CBET-1507469. S.S.H. and R.B., as well as the JHTDB software and hardware infrastructure, were supported in part by the National Science Foundation under Grants No. CMMI-0941530, No. ACI-1261715, No. OCI-1244820, and No. AST-0939767 and Johns Hopkins University's Institute for Data Intensive Engineering & Science.

[1] G. I. Taylor, Production and dissipation of vorticity in a turbulent fluid, Proc. R. Soc. London Ser. A **164**, 15 (1938).

[2] A. Tsinober, *An Informal Conceptual Introduction to Turbulence*, 2nd ed. (Springer, Berlin, 2009).

[3] M. Holzner, M. Guala, B. Luthi, A. Liberzon, N. Nikitin, W. Kinzelbach, and A. Tsinober, Viscous tilting and production of vorticity in homogeneous turbulence, Phys. Fluids **22**, 061701 (2010).

[4] W. T. Ashurst, A. R. Kerstein, R. M. Kerr, and C. H. Gibson, Alignment of vorticity and scalar gradient with strain rate in simulated Navier-Stokes turbulence, Phys. Fluids **30**, 2343 (1987).

[5] S. S. Girimaji and S. B. Pope, Material-element deformation in isotropic turbulence, J. Fluid Mech. **220**, 427 (1990).
[6] M. Guala, B. Luthi, A. Liberzon, A. Tsinober, and W. Kinzelbach, On the evolution of material lines and vorticity in homogeneous turbulence, J. Fluid Mech. **533**, 339 (2005).
[7] J. Bec, L. Biferale, G. Boffetta, M. Cencini, S. Musacchio, and F. Toschi, Lyapunov exponents of heavy particles in turbulence, Phys. Fluids **18**, 091702 (2006).
[8] Y. Li and C. Meneveau, Material deformation in a restricted Euler model for turbulent flows: Analytic solution and numerical tests, Phys. Fluids **19**, 015104 (2007).
[9] P. E. Hamlington, J. Schumacher, and W. J. A. Dahm, Local and nonlocal strain rate fields and vorticity alignment in turbulent flows, Phys. Rev. E **77**, 026303 (2008).
[10] L. Biferale, A. Scagliarini, and F. Toschi, On the measurement of vortex filament lifetime statistics in turbulence, Phys. Fluids **22**, 065101 (2010).
[11] L. Biferale, C. Meneveau, and R. Verzicco, Deformation statistics of sub-Kolmogorov-scale ellipsoidal neutrally buoyant drops in isotropic turbulence, J. Fluid Mech. **754**, 184 (2014).
[12] P. L. Johnson and C. Meneveau, Large-deviation joint statistics of the finite-time Lyapunov spectrum in isotropic turbulence, Phys. Fluids **27**, 085110 (2015).
[13] P. L. Johnson and C. Meneveau, Large-deviation statistics of vorticity stretching in isotropic turbulence, Phys. Rev. E **93**, 033118 (2016).
[14] S. Kramel, S. Tympel, F. Toschi, and G. A. Voth, Preferential Rotation of Chiral Dipoles in Isotropic Turbulence, Phys. Rev. Lett. **117**, 154501 (2016).
[15] A. N. Kolmogorov, The local structure of turbulence in incompressible viscous fluid for very large Reynolds numbers, Dokl. Akad. Nauk SSSR **30**, 299 (1941).
[16] A. N. Kolmogorov, A refinement of previous hypotheses concerning the local structure of turbulence in a viscous incompressible fluid at high Reynolds number, J. Fluid Mech. **13**, 82 (1962).
[17] A. M. Oboukhov, Some specific features of atmospheric tubulence, J. Fluid Mech. **13**, 77 (1962).
[18] E. Balkovsky, A. Fouxon, and V. Lebedev, Turbulent dynamics of polymer solutions, Phys. Rev. Lett. **84**, 4765 (2000).
[19] F. Bagheri, D. Mitra, P. Perlekar, and L. Brandt, Statistics of polymer extensions in turbulent channel flow, Phys. Rev. E **86**, 056314 (2012).
[20] C. M. White and M. G. Mungal, Mechanics and prediction of turbulent drag reduction with polymer additives, Annu. Rev. Fluid Mech. **40**, 235 (2008).
[21] I. Procaccia, V. S. L'Vov, and R. Benzi, Colloquium: Theory of drag reduction by polymers in wall-bounded turbulence, Rev. Mod. Phys. **80**, 225 (2008).
[22] G. Haller, Distinguished material surfaces and coherent structures in three-dimensional fluid flows, Physica D **149**, 248 (2001).
[23] M. A. Green, C. W. Rowley, and G. Haller, Detection of lagrangian coherent structures in three-dimensional turbulence, J. Fluid Mech. **572**, 111 (2007).
[24] G. Haller, Langrangian coherent structures, Annu. Rev. Fluid Mech. **47**, 137 (2015).
[25] R. Maniero, O. Masbernat, E. Climent, and F. Risso, Modeling and simulation of inertial drop break-up in a turbulent pipe flow downstream of a restriction, Int. J. Multiphase Flow **42**, 1 (2012).
[26] H. Yu, K. Kanov, E. Perlman, J. Graham, E. Frederix, R. Burns, A. Szalay, G. Eyink, and C. Meneveau, Studying Lagrangian dynamics of turbulence using on-demand fluid particle tracking in a public turbulence database, J. Turbul. **13**, N12 (2012).
[27] J. Bec, L. Biferale, A. S. Lanotte, A. Scagliarini, and F. Toschi, Turbulent pair dispersion of inertial particles, J. Fluid Mech. **645**, 497 (2010).
[28] G. Eyink, E. Vishniac, C. Lalescu, H. Aluie, K. Kanov, K. Bürger, R. Burns, C. Meneveau, and A. Szalay, Flux-freezing breakdown in high-conductivity magnetohydrodynamic turbulence, Nature (London) **497**, 466 (2013).
[29] K. Kanov and R. Burns, in *Proceedings of the International Conference for High Performance Computing, Networking, Storage, and Analysis, Austin, 2015* (ACM, New York, 2015), Article 43.
[30] J. Graham, K. Kanov, X. I. A. Yang, M. K. Lee, N. Malaya, R. Burns, G. Eyink, R. D. Moser, and

C. Meneveau, A Web Services-accessible database of turbulent channel flow and its use for testing a new integral wall model for LES DNS approach and simulation parameters, J. Turbul. **17**, 181 (2016).

[31] J. Jiménez, Cascades in wall-bounded turbulence, Annu. Rev. Fluid Mech. **44**, 27 (2012).

[32] J. M. Greene and J.-S. Kim, The calculation of Lyapunov spectra, Physica D **24**, 213 (1987).

[33] M. Chertkov, Polymer Stretching by Turbulence, Phys. Rev. Lett. **84**, 4761 (2000).

[34] G. Paladin and A. Vulpiani, Anomalous scaling laws in multifractal objects, Phys. Rep. **156**, 147 (1987).

[35] J. Gartner, On large deviations from the invariant measure, Theory Probab. Appl. **22**, 24 (1977).

[36] R. S. Ellis, Large deviations for a general class of random vectors, Ann. Probab. **12**, 1 (1984).

[37] Y. Li, E. Perlman, M. Wan, Y. Yang, C. Meneveau, R. Burns, S. Chen, A. Szalay, and G. Eyink, A public turbulence database cluster and applications to study Lagrangian evolution of velocity increments in turbulence, J. Turbul. **9**, 1 (2008).

[38] E. Perlman, R. Burns, Y. Li, and C. Meneveau, in *Proceedings of the 2007 ACM/IEEE Conference on Supercomputing, SC '07, Reno, 2007* (ACM, New York, 2007), Article 23.

[39] G. S. Patterson and S. A. Orszag, Spectral calculations of isotropic turbulence: Efficient removal of aliasing interactions, Phys. Fluids **14**, 2538 (1971).

[40] M. Lee, N. Malaya, and R. D. Moser, in *Proceedings of the International Conference for High Performance Computing, Networking, Storage, and Analysis, Denver, 2013* (ACM, New York, 2013), Article 61.

[41] J. Kim, P. Moin, and R. Moser, Turbulence statistics in fully developed channel flow at low Reynolds number, J. Fluid Mech. **177**, 133 (1987).

[42] S. A. Orszag, On the elimination of aliasing in finite difference schemes by filtering high-wavenumber components, J. Atmos. Sci. **28**, 1074 (1971).